

Symmetry-breaking induced surface magnetization in nonmagnetic RuO<sub>2</sub>Dai Q. Ho <sup>1,2,\*</sup>, D. Quang To <sup>1</sup>, Ruiqi Hu <sup>1</sup>, Garnett W. Bryant <sup>3,4,†</sup> and Anderson Janotti <sup>1,‡</sup><sup>1</sup>*Department of Materials Science and Engineering, University of Delaware, Newark, Delaware 19716, USA*<sup>2</sup>*Faculty of Natural Sciences, Quy Nhon University, Quy Nhon 55113, Vietnam*<sup>3</sup>*Nanoscale Device Characterization Division and Joint Quantum Institute, National Institute of Standards and Technology, Gaithersburg, Maryland 20899-8423, USA*<sup>4</sup>*Joint Quantum Institute, University of Maryland, College Park, Maryland 20742, USA*

(Received 28 February 2025; accepted 30 July 2025; published 8 September 2025)

Altermagnetism is a newly identified phase of magnetism distinct both from ferromagnetism and antiferromagnetism. RuO<sub>2</sub> has been considered a prototypical metallic altermagnet with a critical temperature higher than room temperature. Previous interpretations of unusual magnetic properties of RuO<sub>2</sub> relied on the theoretical prediction that local moments on two Ru sublattices, which are connected by fourfold rotational symmetry, are quite significant ( $\approx 1 \mu_B$ ), leading to long-range antiferromagnetic order. However, accumulated experimental data suggest that local moments on Ru in RuO<sub>2</sub> are vanishingly small, indicating the bulk material is likely nonmagnetic. This observation is consistent with the delocalized nature of the 4*d* electron of Ru and the strong screening effect in the metallic state. In this work, we show that despite the nonmagnetic ground state in the bulk, the RuO<sub>2</sub>(110) surface exhibits spontaneous magnetization, which we attribute to the breaking of local symmetry, resulting in electronic redistribution and magnetic moment enhancement. The emergence of surface magnetism gives rise to interesting spectroscopic phenomena, including spin-polarized surface states, spin-polarized scanning probe microscopy images, and potentially spin-dependent transport effects. These highlight the important role of surface magnetic structures in the otherwise nonmagnetic bulk RuO<sub>2</sub>.

DOI: [10.1103/PhysRevMaterials.9.094406](https://doi.org/10.1103/PhysRevMaterials.9.094406)

## I. INTRODUCTION

Altermagnetism (AM) is an emerging phase of magnetism that differs from the well-known ferromagnetism (FM) and antiferromagnetism (AFM) [1]. In altermagnetic materials, spin-splitting in the electronic band structure occurs alternately in reciprocal space directions that are related to each other by rotation or reflection but not translation or inversion, which is determined by the presence of nonmagnetic ligands in real space [1]. Among the earliest and most studied candidates for altermagnetic materials is RuO<sub>2</sub>, which has been considered a prototype altermagnet [1,2]. Despite various theoretically predicted [2] and experimentally observed phenomena linked to time-reversal symmetry breaking in AM such as the anomalous Hall effect [3], spin-splitter effect [4], and magnetic circular dichroism [5], ascribed to the assumption that RuO<sub>2</sub> is an AM with a high Néel temperature and a significant local moment (typically assumed  $\approx 1 \mu_B$  in theoretical calculations), direct experimental evidence for such a high moment in this 4*d* metallic oxide is lacking. Therefore, the magnetic configuration of RuO<sub>2</sub> and especially the presence of local moments and long-range magnetic ordering are still subjects of debate [6]. The first neutron scattering experiment on RuO<sub>2</sub> reported a local moment of only  $0.05 \mu_B$  [7]. Subsequently, an experiment using the resonant x-ray scattering technique supported

the AFM ground state in RuO<sub>2</sub> [8]. However, recent in-depth investigations strongly suggest that the ground state of RuO<sub>2</sub> is nonmagnetic/paramagnetic [9–14]. For instance, local-moment-sensitive muon spin rotation ( $\mu$ SR) and neutron diffraction experiments have shown that the ground state of the bulk RuO<sub>2</sub> is likely nonmagnetic, with negligibly small local moments of  $10^{-4} \mu_B$  [9,11]. Furthermore, by using broadband infrared spectroscopy combined with first-principles calculations to probe the optical conductivity of RuO<sub>2</sub>—a bulk electronic property—researchers concluded that bulk RuO<sub>2</sub> is well described by a nonmagnetic model [13]. Very recently, people have directly probed the electronic structure of RuO<sub>2</sub> in bulk and thin film samples using angle-resolved photoemission spectroscopy (ARPES) and found no evidence of spin splitting in the electronic structure of the material [10,14]. These findings align with the delocalization and weak correlation nature of the Ru 4*d* orbitals, consistent with the metallic property of the compound.

Most of the experiments mentioned above have been concentrated on bulk or thin films, with less focus on surface properties. However, the surface properties of altermagnets might play a significant role in various phenomena at surfaces and interfaces or even be key to explaining some observations [15,16]. Of many low-index surfaces, RuO<sub>2</sub> surface and thin films in the crystallographic direction  $\langle 110 \rangle$  are of particular interest since that is the crystal surface with the lowest surface energy and with easy cleavage [17,18]. For example, the RuO<sub>2</sub>(110) surface has been a primary focus in catalysis research thanks to its high electrocatalytic water splitting activity, attributed to the presence of Ru

\*Contact author: [daiqho@udel.edu](mailto:daiqho@udel.edu)†Contact author: [garnett.bryant@nist.gov](mailto:garnett.bryant@nist.gov)‡Contact author: [janotti@udel.edu](mailto:janotti@udel.edu)

dangling bonds [17,19]. However, most studies have ignored the magnetic properties of the surface, except for a couple of theoretical predictions, which highlighted the role of surface magnetism in  $\text{RuO}_2(110)$  in catalytic reactions during electrolysis [20,21]. Given the subtlety of magnetism in  $\text{RuO}_2$  seen in the literature, it is possible that surface effects could be a relevant source of magnetic phenomena observed in various samples. For instance, strained  $\text{RuO}_2(110)$  thin films grown on  $\text{TiO}_2$  substrates have recently been shown to exhibit superconducting behavior at low temperatures and a metal-to-insulator transition in the ultrathin limit regime [22–24]. The role of the soft-phonon mode and the enhancement of electron density at the Fermi level ( $E_F$ ) have been invoked to explain this superconductivity. However, the possible role of the magnetic structure in supporting these phenomena has been overlooked.

As noted previously, Torun *et al.* [20] have predicted that surface magnetization can spontaneously develop on the  $\text{RuO}_2(110)$  surface. However, their study was not without limitations. First, the slab used in their calculations, consisting of only five layers of  $\text{RuO}_2$ , was probably insufficient to accurately represent both surface and bulk-like regions, potentially affecting the predicted behavior of surface magnetization. In metallic systems such as  $\text{RuO}_2$ , the electronic wave functions of the top and bottom surfaces of the slab used in the calculation can penetrate deep into the bulk and mutually interact if the slab is not sufficiently thick, leading to an alteration of the electronic properties of the true surface. Second, the origin of the surface magnetism was not comprehensively explored. More importantly, since their work focused on surface catalysis, it did not address how surface magnetization influences electronic and magnetic properties that are critical for spectroscopic and transport phenomena, which is highly relevant for spintronics applications [5,25].

In this paper, using first-principles calculations based on density functional theory (DFT), we show that surface magnetism spontaneously develops in  $\text{RuO}_2(110)$ . The spontaneous surface magnetization can be understood from the breaking of symmetry on the surface of  $\text{RuO}_2(110)$ , leading to a significant reconstruction of the electronic structure of  $\text{RuO}_6$  octahedra at the surface layer, i.e., in the band filling of the Ru  $4d$  orbitals, resulting in sizable local moments. Remarkably, the presence of spontaneous surface magnetization leads to spin-polarized surface states and spin-dependent transport effects. These results can be important for understanding the experimental data on  $\text{RuO}_2$  obtained using spectroscopic and transport measurements such as spin- and angle-resolved photoemission spectroscopy (S-ARPES) [10,26], spin-polarized scanning tunneling microscopy/spectroscopy (SP-STM/SP-STs), anomalous Hall measurements [3], and interfacial spin-dependent transport phenomena [27].

## II. COMPUTATIONAL METHOD

Our calculations are based on DFT [28,29] and the projector augmented wave (PAW) method was employed to treat interactions between the valence electrons and the ionic cores [30,31] as implemented in the VASP code [32–34]. We used the recommended standard PAW potentials for Ru and O,  $\text{Ru}_{\text{pv}} (4p^6 4d^7 5s^1)$  and  $0 (2s^2 2p^4)$ . Bloch wave

functions of the materials were expanded in a plane-wave basis set with a cutoff energy of 600 eV. Due to the metallic nature of  $\text{RuO}_2$ , the Methfessel-Paxton smearing method ( $\text{ISMEAR} = 1$ ) in combination with a smearing value of 0.2 eV was used for integration over the Brillouin zone (BZ) when optimizing structural parameters. For very accurate total energy calculations, we utilized the tetrahedron method with Blöchl corrections ( $\text{ISMEAR} = -5$ ) and a Gamma-centered  $k$ -point mesh to sample the BZ. Due to the recent experimental observation of a nonmagnetic ground state in bulk  $\text{RuO}_2$  [9–14], we employed the PBE +  $U$  approach with  $U = 0$  [6,35–37] to describe its electronic structure. Additionally, since spin-orbit coupling (SOC) does not significantly affect the electronic and magnetic structures of  $\text{RuO}_2$ , it was neglected in our calculations. Data postprocessing was conducted in part with the help of VASPKIT [38].

Bulk  $\text{RuO}_2$  was simulated using a tetragonal unit cell with a rutile structure ( $P4_2/mnm$ , SG 136). Due to the metallic property of bulk  $\text{RuO}_2$ , a dense  $k$ -point mesh of  $12 \times 12 \times 18$  was used to sample the bulk BZ. The lattice constant was adopted from a recent experimental determination [39]. To gain insight into the magnetic structure of the  $\text{RuO}_2(110)$  surface, we performed calculations using the slab model with 3D periodic boundary conditions.  $\text{RuO}_2$  films along [110] were built by reorienting the lattice vectors of the primitive cell, i.e., primitive lattice vectors along [001],  $[1\bar{1}0]$ , and [110] become [100], [010], and [001] of the  $\text{RuO}_2(110)$  surface unit cell, respectively. We chose stoichiometric slabs with an odd number of Ru layers. These slabs are nonpolar, eliminating unnecessary complications related to asymmetric structures, such as spurious charge transfer, and build up electric fields across the slab thickness. A  $k$ -point mesh of  $12 \times 6 \times 1$  was used for structural optimization of the surface unit cell, and a denser mesh of  $18 \times 9 \times 1$  was used for density of states (DOS) calculations. To eliminate spurious image interactions between slabs, a vacuum space of at least 20 Å was added to the slab normal direction. Atomic positions were fully relaxed until the Hellman-Feynman force on each atom was smaller than 0.005 eV/Å while keeping the in-plane lattice vectors fixed to the experimental bulk values. To assess the impact of unit cell size and shape on the development of surface magnetization, we performed test calculations allowing the unit cell to vary. These tests showed negligible influence, so the unit cell size and shape were also kept fixed during atomic relaxation. Further details on the effects of full unit cell relaxation on magnetic structures can be seen in the Supplemental Material (SM), Fig. S1 [40].

To gain insights into the chemical bonding between atomic pairs contributing to the emergence of spin-polarized states at the surface of  $\text{RuO}_2$ , we performed a crystal orbital Hamilton population (COHP) analysis [41,42]. The COHP method decomposes the one-particle band energies into interactions between atomic orbitals of adjacent atoms. It effectively weighs the DOS by the corresponding Hamiltonian matrix elements, thus recovering the phase information of calculated wave functions that is otherwise missing in the band structure or DOS descriptions of material electronic structures. This enables the identification of bonding, nonbonding, and antibonding characteristics among the pairwise atoms. The stability of these interactions is quantified by the COHP

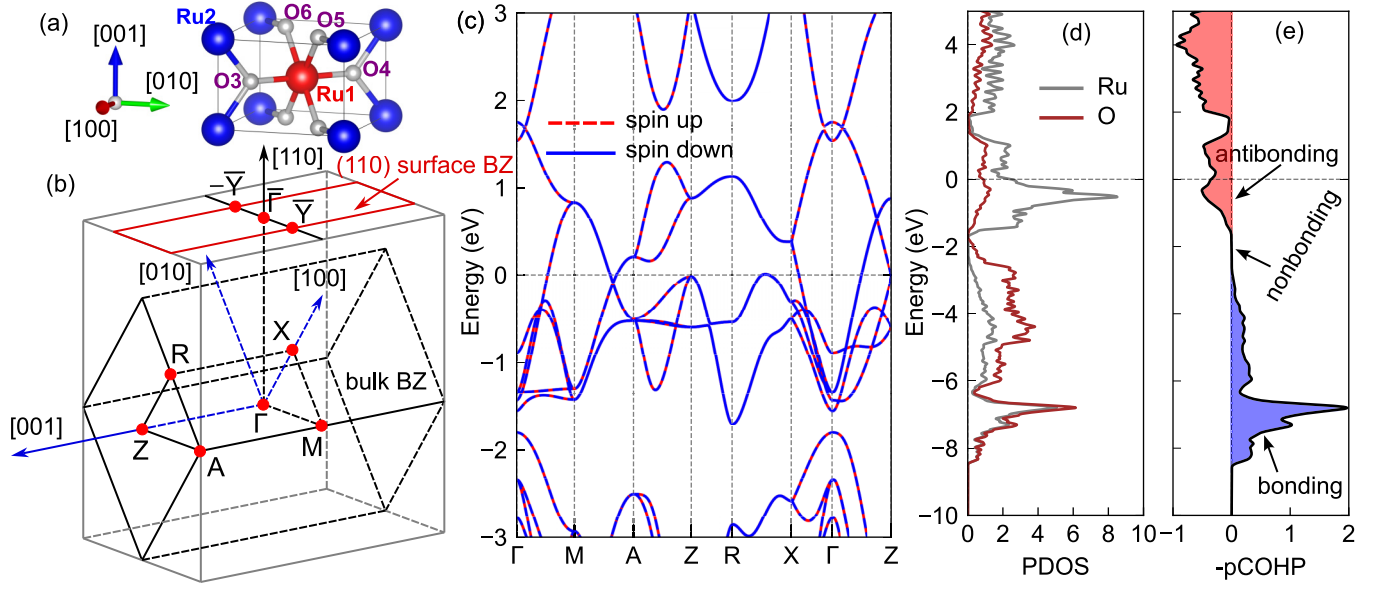


FIG. 1. Crystal structure, electronic structure, and chemical bonding analysis of bulk  $\text{RuO}_2$ . (a) Rutile structure of  $\text{RuO}_2$  with two Ru sublattices: Ru-center (red) and Ru-corner (blue), oxygen (silver); O3, O4 are apical ligands of Ru1 and the rest are equatorial ones, (b) bulk Brillouin zone (bulk BZ) shown in black and rotated so that the [110] crystallographic direction pointing upwards and normal to the (110) surface whose BZ shown in red; note that electronic states of the 3D bulk will be projected onto the 2D BZ of the surface when comparing electronic structure of the slab and the bulk, i.e.,  $\Gamma$  to  $\bar{\Gamma}$ , X to  $\bar{Y}$ , M to neighboring  $\bar{\Gamma}$ , etc. (c) spin-polarized electronic band structure of the bulk exhibiting no spin-polarization ( $E_F$  set to 0), (d) projected density of states on Ru and O in bulk, and (e) the corresponding  $-\text{pCOHP}$  curve on the same energy scale.

values. A positive COHP value indicates bonding interactions, while a negative value represents an antibonding character. Traditionally, COHP analysis was done directly from atom-centered basis set calculations. However, since our calculations were done using the plane-wave basis set, a projection scheme from this basis set to a local orbital basis set was employed using the LOBSTER code [41–43]. In this projection scheme, the equivalence of the traditional COHP quantity is  $-\text{pCOHP}$  (negative of projected COHP). Our study applied COHP analysis to examine the bonding character and stability of nearest-neighboring atomic pairs around Ru atoms on the surface and in bulk-like regions. For the projection, we employed the local basis function as defined in `pbeVaspFit2015`.

Since spin-polarized scanning tunneling microscopy (SP-STM) can be used to recognize spin polarization effects on the surface [44], we simulated spin-resolved STM images employing the Tersoff-Hamann approximation [45]. In this approach, the tunneling current at the simulated probe tip (i.e., at a particular distance from the surface) in an STM experiment is proportional to the local density of states (LDOS) of the integrated electronic states ranging from the Fermi level to a predefined energy level given by a bias voltage  $V$ , roughly corresponding to an experimental voltage. The LDOS is given by

$$n(r, E) = \sum_i |\psi_i(r)|^2 \delta(\varepsilon_i - E), \quad (1)$$

and the tunneling current can be expressed as

$$I(r, V) \propto \int_{E_F}^{E_F + eV} n(r, E) dE, \quad (2)$$

where  $n(r, E)$  represents the LDOS at a given position  $r$  and energy  $E$ . The LDOS can be evaluated from partial charge densities calculated from a preconverged wave function. The partial charge density file from VASP was read by the HIVE-STM program [46], and STM images were generated using the constant-height method (at a height of  $\approx 3 \text{ \AA}$  above the highest atoms of the slab—the oxygen bridging atoms). For a given bias  $V$ , the simulated STM images reflect the contrast in the partial charge densities within the energy range  $0 < E - E_F < V$  (for  $V > 0$ , positive bias) and  $V < E - E_F < 0$  (for  $V < 0$ , negative bias).

### III. RESULTS AND DISCUSSION

#### A. Electronic and magnetic properties of bulk $\text{RuO}_2$

The calculated electronic band structure of the bulk, taking into account the spin-polarization effect shown in Fig. 1(c), does not exhibit spin polarization. On the contrary, the assumed altermagnetic state exhibits significant spin splitting ( $> 1 \text{ eV}$ ) lying along the  $\Gamma$ -M high-symmetry path of the bulk Brillouin zone (BZ) as described by band structure calculations with relatively large on-site Hubbard  $U$  values ( $U \approx 1.5 - 2 \text{ eV}$ ) [2,7]. However, this spin splitting does not appear in the nonmagnetic state. Along this momentum direction, three bands are present near the Fermi level, with an additional flat band lying around  $-1.5 \text{ eV}$  below the Fermi level. When considering the electronic structure of the (110) slab, the  $\Gamma$ -M path of the bulk BZ is of particular importance since bulk band dispersions along this path and parallel to it are projected onto the high-symmetry path  $\bar{\Gamma}$ - $\bar{Y}$  of the surface BZ, as illustrated in Fig. 1(b).

TABLE I. Atomic charge states of Ru and O atoms in the bulk and at the surface layer obtained with different population methods.

Population method	Bulk			Surface layer				
	Ru	apical-O	equatorial-O	Ru-5f	Ru-6f	O-br	O-3f	O-sub
Bader	1.74	-0.87	-0.87	1.60	1.81	-0.75	-0.89	-0.90
Mulliken	1.38	-0.69	-0.69	1.39	1.52	-0.61	-0.75	-0.76
Löwdin	1.20	-0.60	-0.60	1.19	1.32	-0.54	-0.64	-0.67

The DOS and chemical bonding analysis, shown in Figs. 1(d) and 1(e), highlight important characteristics of Ru–O bonds in RuO<sub>2</sub>. The DOS in Fig. 1(d) clearly shows strong hybridization between the Ru and O orbitals over a wide range of energy. Notably, between 8 and 6 eV below the Fermi level, pronounced peaks in the atomic-projected density of states (PDOS) and  $-p\text{COHP}$  (positive—bonding character) with similar contributions from both Ru and O indicate a strong covalent bonding, best described by the  $\sigma$ -bonding composed of Ru  $4d$  ( $e_g$ ) and O  $2p$  orbitals [47]. In addition, approximately from 6 eV to 3 eV below the Fermi level, small positive values of  $-p\text{COHP}$ , with a greater contribution of oxygen, suggest a weaker covalent bonding character of the Ru–O bonds due to the  $\pi$ -bonding between Ru  $4d$  ( $t_{2g}$ ) and O  $2p$ . Around  $-2$  eV, the contribution of Ru disappears, i.e., Ru PDOS is zero, leaving only O  $2p$  states. This indicates that the electrons occupying these states belong to nonbonding orbitals and do not contribute to the Ru–O bonding strength, leading the  $-p\text{COHP}$  values to approach zero. These characteristics suggest strong mixed covalency and ionicity in Ru–O bonds, which is consistent with the atomic charge states of Ru and O obtained from population analysis based on charge density using the Bader charge method via the atom-in-molecule (AIM) approach [48,49] or wave function-based methods such as Mulliken [50] and Löwdin [51] charges obtained within the projection scheme of the LOBSTER code [52]. The charge states of the atoms determined from these analyses are lower in magnitude than the formal values of  $+4$  for Ru and  $-2$  for O, as shown in Table I.

Interestingly, in the vicinity of the Fermi level, i.e., from  $-2$  eV to 2 eV, the contribution of Ru  $4d$  becomes dominant and populates antibonding crystal orbitals, as indicated by negative  $-p\text{COHP}$  values. This implies potential instability when electrons occupy these states. Fortunately, the DOS and  $-p\text{COHP}$  peaks lie approximately 0.5 eV below the Fermi level, alleviating the instability due to filling antibonding orbitals [53,54]. Ultimately, despite the presence of antibonding Ru–O interactions near the Fermi level in the  $-p\text{COHP}$  curves, the integrated values of  $-p\text{COHP}$  for Ru–O bonds ( $-Ip\text{COHP}$  values) are positive (see SM, Table S1 [40]), indicating a net bonding character for these interactions. Consequently, from a chemical perspective, there is no driving force for electronic reconstruction (i.e., the redistribution of the two spin channels), resulting in a stable, nonmagnetic ground state rather than an ordered magnetic one. Despite the nonmagnetic character of bulk RuO<sub>2</sub>, intriguing phenomena can arise at the (110) surface, leading to the emergence of surface magnetism. In the next section, we will explore how these localized states, influenced by surface geometry and reduced coordination, contribute to the overall magnetic behavior of the (110) surface.

## B. Magnetization on RuO<sub>2</sub>(110) surface

### 1. Emergence of surface magnetization

The converged relaxed 13-layer slab unit cell (13L) is shown in Fig. 2(a). This symmetric structure represents both bulk and surface regions since it is thick enough to decouple the two surfaces, and the middle layer behaves as a bulk-like region (see SM, Fig. S2 [40] for the dependence of local moments of surface Ru atoms and top-layer magnetization on slab thickness). Each layer stacked along the [110] direction contains two Ru atoms corresponding to the Ru-center and Ru-corner sublattices of the bulk [cf. Fig. 1(a)]. This arrangement would yield a magnetically compensated structure with oppositely pointed moments within each (110) plane if the ground state of the bulk were antiferromagnetically ordered with the Néel vector along [001], as assumed earlier—similar to the case of the isostructural FeF<sub>2</sub> antiferromagnet [55].

In contrast to the bulk, local moments develop on the surface layers of the slab, decaying rapidly into the bulk. The collinear moments arrange ferrimagnetically within the surface layers, with unequal spin moments: Ru-center ( $\approx 0.61 \mu_B$ ) and Ru-corner ( $\approx -0.17 \mu_B$ ) couple collinearly in opposite directions. The majority spin density is located primarily on the Ru-center atom (denoted Ru-6f due to its six-fold coordination) and bridging oxygen (O-br, spin moment  $\approx 0.19 \mu_B$ ), while the Ru-corner atom (denoted Ru-5f due to its fivefold coordination) dominates the minority spin density counterpart [cf. Fig. 2(b) for detailed labeling of atomic surface atoms]. Other oxygen ligands of the outermost layers exhibit non-spin-polarized behavior [Fig. 2(a)]. Notably, the induced surface magnetization in RuO<sub>2</sub>(110) reaches a substantial value of  $\approx 3.0 \mu_B/\text{nm}^2$ —two orders of magnitude larger than the predicted magnetization in the isostructural rutile FeF<sub>2</sub> [55], despite the latter exhibiting an intrinsic AFM ordering.

As seen in Fig. 2(a) and evidenced by variations in the local moments for each Ru sublattice across layers, the magnetization density decreases dramatically from the surface layer to the innermost (bulk-like) layers. Local moments on Ru, and consequently the layer magnetization, nearly vanish starting from the layer just beneath the surface [Fig. 2(c), bottom panel]. The emergence of surface-layer magnetism and the rapid decrease in magnetization can also be observed in the layer-projected DOS in Fig. 2(e), where significant spin splitting is shown to occur mainly on the top layer. This magnetic structure is lower in energy than the nonmagnetic counterpart by  $\approx 45$  meV per unit cell, independent of the slab thickness, consistent with the origin of the magnetic structure being solely due to the surface layer (see SM, Fig. S3 [40] for the relative energy of the spin-polarized state compared to the non-spin-polarized counterpart as a function of slab thickness).

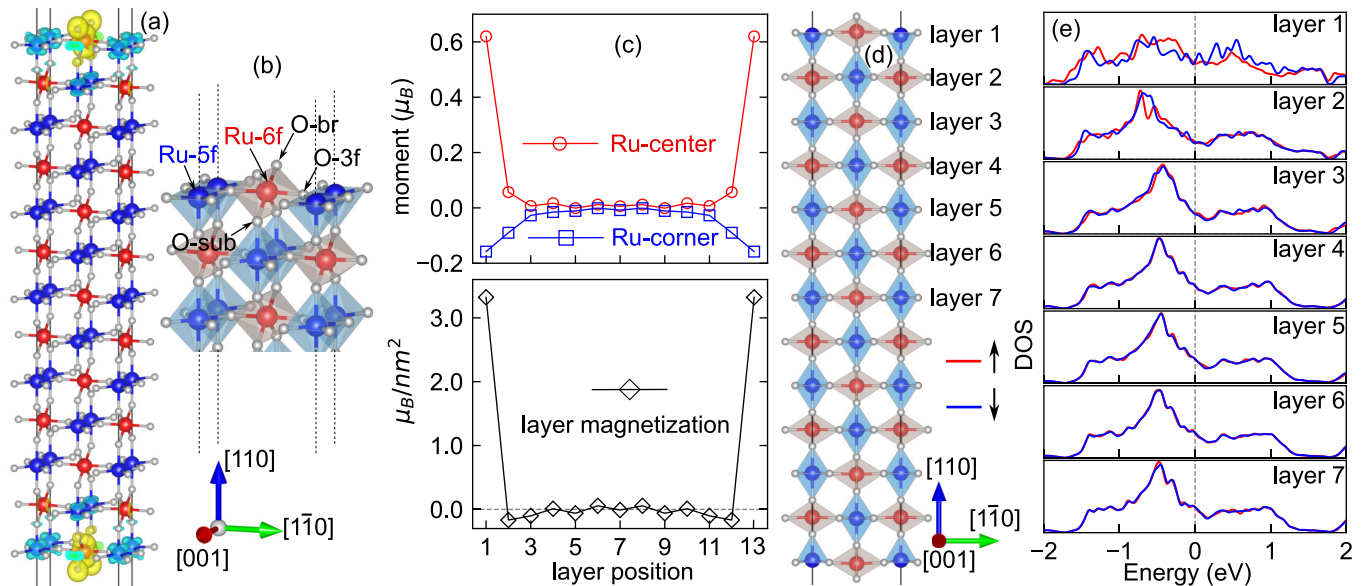


FIG. 2. Geometrical structure of the (110) surface and the emergence of surface magnetism in the 13L slab. (a) The slab structure of 13L  $\text{RuO}_2(110)$  includes two Ru sublattices inherited from the bulk: Ru-center in red, Ru-corner in blue, and oxygen ligands in silver. At the surface layers, Ru-center atoms are fully octahedrally coordinated by six O ligands (denoted as Ru-6f), while the Ru-corner sublattice has one dangling bond due to surface termination (Ru-5f), see (b) for a better view. Also shown is the magnetization density visualization, which exhibits significant accumulation of spin moments only at the outermost layers, with spin-up in yellow and spin-down in cyan. The isosurfaces are plotted using the 5% of the maximum isosurface value. (b) Detailed atomic structure of the surface includes stoichiometric surface termination, with labels for atoms in the surface layer. (c) The spin moment at each Ru site in each layer (top panel), and the magnetization of each layer (bottom panel) as functions of the positions of the layer in the slab. (d) View along the [001] direction showing the layers numbered for the layer-projected DOS in (e), demonstrating that spin polarization decays quickly when approaching inner layers.

In a recent study, Weber *et al.* [55] demonstrated that surface magnetization can spontaneously emerge at the surface of an antiferromagnet with suitable symmetry, including the (110) surface of an AFM with a rutile structure, such as  $\text{FeF}_2$ , which is isostructural to  $\text{RuO}_2$ . Accordingly, surface magnetization is intrinsically linked to the magnetic structure of the bulk. However, as shown above, surface magnetization also arises from the local breaking of bulk symmetry at the surface of a nonmagnetic material. Further, we want to emphasize that the surface magnetism seen in our simulation is robust with DFT functionals as long as the functional gives rise to nonmagnetic bulk state, i.e., those PBE +  $U$  with the on-site  $U$  values not exceeding 1.06 eV [6]. Thus, the presence of surface magnetization alone does not constitute a necessary or sufficient condition to infer the bulk magnetic structure. Bulk measurements are required to identify the magnetic domain conclusively.

## 2. The cause of surface magnetization in $\text{RuO}_2(110)$

In this section, we investigate the origin of surface magnetization on  $\text{RuO}_2(110)$ , considering the nonmagnetic bulk state. From bulk  $\text{RuO}_2$  to the (110) surface, the symmetry of the already distorted octahedron around the Ru-corner and Ru-center atoms of the surface layers is further reduced due to surface termination. The Ru-corner (Ru-5f) loses one of its apically coordinated oxygen ligands, while the Ru-center (Ru-6f) maintains its coordination number. The two bridging oxygen ligands on the surface, which coordinate equatorially to the Ru-6f atom, become covalently *unsaturated* with only

two bonds remaining as compared to three bonds in the bulk, contributing to structural distortions that affect the hybridization between Ru 4d and O 2p states. These distortions are expected to lift the degeneracy of the Ru 4d states further. Without any surface relaxation, i.e., no structural relaxation performed for slabs, the local symmetry of the Ru-5f is  $C_{4v}$  (square pyramidal), while the Ru-6f retains its distorted octahedral symmetry as in the bulk. Nevertheless, this configuration is unstable, leading to structural relaxation akin to a Jahn-Teller distortion, which further lowers the local symmetry around the surface Ru atoms. During this relaxation, the Ru-O apical bonds in the Ru-5f-centered square pyramidal shorten, whereas the apical bonds in the Ru-6f-centered octahedra lengthen. Additionally, the equatorial Ru-O bonds centering around the Ru-6f become asymmetrically distorted; those involving the bridging oxygen ligands are significantly shortened, while the others elongate slightly. Despite these structural reconstructions, the total energy of the system remains high, with a considerable DOS at the Fermi level contributing to the occupation of antibonding states, as illustrated in Fig. 3(a).

To achieve stability, spin polarization is necessary to redistribute electronic densities of the two spin sublattices, resulting in spontaneous surface magnetization as described in the previous section. COHP analysis offers valuable insight into the driving forces behind the emergence of magnetization from a chemical bonding perspective [53,54]. Figure 3 presents the projected density of states (PDOS) on the atoms of the top surface, along with  $-p\text{COHP}$  curves (averaged for the nearest-neighbor Ru-O contacts) for both structurally

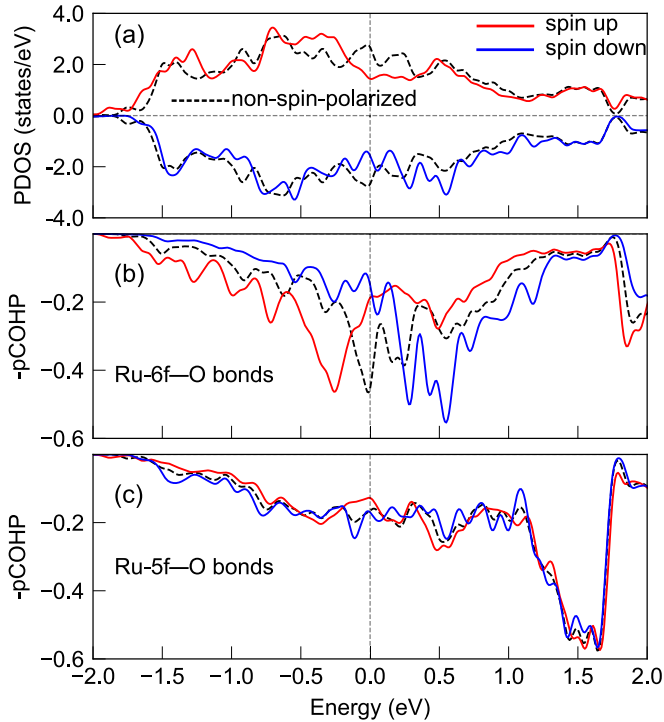


FIG. 3. Chemical bonding analysis for the emergence of surface magnetization. (a) Comparison of PDOS around the Fermi level in the nonmagnetic state, and spin-polarized state of the surface, (b)  $-p\text{COHP}$  curves averaged for Ru-O bonds around the Ru-6f, and (c) around the Ru-5f atoms at the surface ( $E_F$  set to 0).

relaxed nonmagnetic and magnetic states. In the nonmagnetic state, despite the structural relaxation,  $\text{RuO}_2(110)$  displays a peak at the Fermi level in both the PDOS and  $-p\text{COHP}$  (with negative values) curves, indicating an unstable configuration. This suggests that the structural effect alone is not enough to stabilize the surface system. Consequently, the surface exhibited pronounced electronic reorganization upon spin-polarization calculation. The surface atoms become magnetized, and the electronic structure shows substantial spin-polarization [Figs. 2(e) and 3(a)]. Remarkably, this spin-polarized reorganization shifted the DOS and  $-p\text{COHP}$  peaks away from the Fermi level, leading to a drastic decrease in the density of antibonding states at the Fermi level for both spin channels, and effectively stabilizing the system by about 43 meV. The electronic redistribution effect is stronger for Ru-6f compared to that of Ru-5f, thus giving rise to larger moments on the former as seen in the previous section. In addition, when performing further structural relaxation with the inclusion of spin-polarization, we observed no discernible structural difference to the non-spin-polarized case, gaining only 2 meV in total energy. Ultimately, it is the spin-polarization that stabilizes the surface by about 45 meV per unit cell, regardless of the slab thickness, as mentioned in the previous section.

The development of surface magnetization on  $\text{RuO}_2(110)$  can also be understood through the lens of the Stoner criterion, which states that magnetization emerges if the product of the density of states at the Fermi level and the exchange interaction parameter exceeds unity [56]. In the nonmagnetic

state, even after the structural relaxation, the high DOS at the Fermi level suggests the surface instability. This unstable state drives the surface to electronic redistribution, and the system minimizes its energy through spin polarization. This reorganization substantially lowers the DOS for both spin channels around the Fermi level as described above, stabilizing the surface. The significant reduction in antibonding states and the redistribution of electronic density through spin polarization effectively meet the Stoner criterion, leading to spontaneous surface magnetization.

Electronic reconstruction that results in the emergence of induced magnetic moments and net magnetization for the surface layers can be further seen in the variation of charge states of individual atoms at the surface compared to their bulk counterparts, as detailed in Table I. Different population methods yield varying values for these charge states, but the trend of electronic reconstruction for the surface atoms remains consistent across these methods. For example, using the charge density-based Bader approach, we find that the charge state of the Ru-5f atom generally decreases, while that of the Ru-6f atom increases relative to the bulk values. This is primarily due to the absence of one oxygen atom coordination (the apical oxygen) of the Ru-5f, which leads to an increased electron density and a corresponding decrease in charge state at the Ru-5f site. In contrast, the Ru-6f retains full coordination with six oxygen ligands, but also specially interacts with two bridging oxygen ligands having higher hole densities due to one unsaturated coordination for each oxygen. This condition facilitates charge transfer from the Ru-6f to these covalently unsaturated ligands, thereby increasing its charge state. In addition, it is observed that only atoms on the surface or very close to it have their charges significantly modified; charges of other atoms negligibly vary from the bulk values (see SM, Fig. S4 [40]). This further supports the surface origin of magnetism in  $\text{RuO}_2(110)$ .

### 3. The significance of surface magnetism in $\text{RuO}_2(110)$

Surface magnetism developed on the surface of  $\text{RuO}_2(110)$  suggests that we can probe this phenomenon directly, i.e., the spin-splitting effect associated with surface bands should be detectable by surface- and spin-sensitive spectroscopy techniques such as spin-resolved ARPES. Figure 4 shows the slab band structure with weighted contribution from the atoms of the top layer—layer 1 in Fig. 2(d)—along with projected bulk bands in the light gray background. Interestingly, low-energy electronic structures close to the Fermi level exhibit surface states with flatness and significant spin-splitting exchange energy of approximately 0.60 eV, as indicated by black arrows in Figs. 4(a) and 4(b). The occupied flat bands, which lie approximately 0.40 eV below  $E_F$ , are derived from all magnetic atoms of the surface layer, i.e., Ru-6f, O-br, and Ru-5f, which is consistent with previous observation [57] (see SM, Fig. S5 [40]). Other nonmagnetic atoms of the top layer, such as O-3f and O-sub, contribute negligibly to these states. The minority spin counterparts of these flat bands are unoccupied (located 0.20 eV above  $E_F$ ) and dominated by the Ru-6f character with smaller contributions from O-br and Ru-5f (see SM, Fig. S5 [40]). This is consistent with the highest calculated magnetic moment value for the Ru-6f atom among others on the surface.

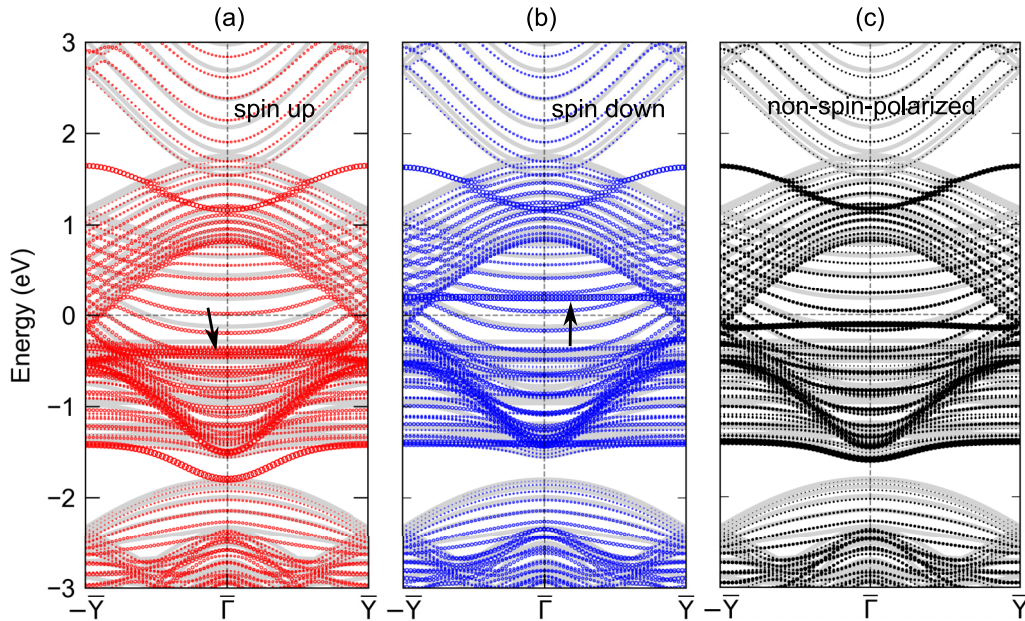


FIG. 4. Projected electronic band structure for the atoms of the outermost layer plotted along the corresponding projected bulk bands shown in the light gray background ( $E_F$  set to 0). Each layer contains two formula units of  $\text{RuO}_2$ . (a) Majority spin (spin up, red), (b) minority spin (spin down, blue), (c) non-spin-polarized band. Surface bands can be seen with high intensity of weighted data, those near the Fermi level pointed to by black arrows. Zoomed-in versions of (a) and (b) near the  $E_F$  can be found in Fig. S7 of the SM [40].

It should be noted that the presence of occupied flat bands near the Fermi level has been observed in previous experiments by using ARPES [10,26,58,59]. However, the spin polarization of these bands and the presence of their spin exchange counterpart above  $E_F$  have not been reported in the literature. This is likely due to the ARPES technique probing only occupied states. Therefore, unoccupied states-sensitive experiments such as inverse ARPES, STM, or x-ray absorption spectroscopy (XAS) might be required to realize the full spin-polarized spectrum of the flat bands in the proximity of the Fermi level due to the surface magnetism in  $\text{RuO}_2(110)$ .

As mentioned above, the existence of flat bands lying closely beneath the Fermi level has been observed experimentally, but the origin of these states is still a debate in the literature. Jovic *et al.* [59] showed that the flat bands have a surface origin. They were considered to be topologically trivial states that connect the projection of nodal lines along the XR directions in the bulk BZ [59]. Very recently, based on spin-resolved ARPES data, Liu *et al.* [10] assigned the flat bands near the Fermi level along the  $\Gamma$ -M momentum direction as surface states. However, a recent experiment has also shown the existence of flat bands along that  $\Gamma$ -M direction, but the authors argued that it likely has a bulk origin [26]. It is noteworthy that our projected bulk spectrum exhibits a few flat bands residing below the Fermi level and overlapping in energy with the flat bands of interest, i.e., those with significant contributions from the outermost layers as described above. This overlap could be the source of confusion in the literature.

To reconcile the origin of these flat bands, we calculated the layer-resolved (projected) band structure for each layer of the slab, and the results are shown in Fig. S6 of the SM [40]. The layer-projected band structures show a rapid decrease in the contribution of each layer to the flat bands of interest when going from the outermost to the innermost (or the middle,

the bulk-like) layer. The middle layer of the slab displays no fingerprint of the pairs of bands being discussed (see SM, Fig. S6(f) [40]), suggesting that these bands are derived from the top and bottom layers (the surface layers). In addition, the charge density associated with the flat bands at the  $\Gamma$  point plotted in Fig. S7 of the SM [40] clearly shows the outermost-layer origin of the bands. The fact that those surface bands are spin-split is clear evidence for the emergence of surface magnetization, mostly due to the atoms at the surface. This is consistent with the observation that the developed local moments on atoms decay quickly when going from the surface to the bulk region.

Another pair of spin-splitting bands can be observed around  $-1.5$  eV where the minority spin channel is completely flat while the majority counterpart is slightly dispersive. This contrasts with the corresponding surface-dominated bands of the nonmagnetic surface, where these bands are also slightly dispersive in the proximity of the  $\Gamma$  point but without spin polarization [Fig. 4(c)]. Similar to the flat band surface states close to the Fermi level, these spin-polarized states split in energy, i.e., one moving up and the other moving down, compared to nonmagnetic states upon spin-polarization calculation. In addition, there is another set of surface states sitting at around 1.5 eV above the Fermi level. These states are slightly dispersive near the  $\Gamma$  point and do not show a significant exchange splitting, likely due to the dominating contribution of the small moment Ru-5f atoms to the band composition.

Considering that the bulk  $\text{RuO}_2$  is nonmagnetic and our calculations exclude relativistic effects, the emergence of significant spin exchange splitting associated with surface bands near the Fermi level underscores the unique feature of the spontaneous surface magnetization of  $\text{RuO}_2(110)$ . This characteristic is likely a key factor in determining the magnetic

properties of surface  $\text{RuO}_2$ . Additionally, the presence of large spin-splitting surface bands, particularly those close to the Fermi level, suggests that the spin polarization of transport at the surface would differ significantly from that in the bulk, which could profoundly influence spin-dependent phenomena in  $\text{RuO}_2$ . Therefore, due to the induced exchange interactions, proximity effect, and potential spin current manipulation at the surface, we conjecture that surface magnetism could play a vital role in the material's spin Hall magnetoresistance when coupled with heavy metals such as Pt or Ta [27], or serve a relevant source for interfacial exchange coupling when paired with a magnetic material.

In the bulk, spin-orbit coupling was neglected due to its small effect. However, local inversion symmetry breaking and atomic relaxation at the surface may lead to enhanced SOC effect, resulting in intriguing phenomena, especially when coupled with the spin-polarization effect at the surface as described above. Although we have not included SOC in our calculations, we expect it to generate modest magnetocrystalline anisotropy, resulting in a *soft magnetic* system that may slightly influence surface magnetic properties without fundamentally altering the collinear ferrimagnetic spin structure observed in our spin-polarized calculation. In addition, enhanced SOC effect at the surface could further enlarge the spin splitting already seen in our spin-polarized calculations, and introduce Rashba-type splitting and spin textures. We note, however, that the electronic structures near the Fermi level are inherently complex due to their metallic nature, which may complicate the analysis of SOC-induced spin polarization and spin textures.

Surface magnetization can also exhibit different characteristics when probed by surface- and spin-sensitive microscopy techniques such as spin-polarized STM [60]. Since SP-STM is applicable to electrically conductive materials, such as magnetic metals or doped semiconductors,  $\text{RuO}_2$ 's metallic nature makes it a suitable candidate for the technique. The general observation from STM images shown in Fig. 5 is the high intensity at bright spots corresponding to the O-br-derived electronic states due to their positions lying closest to the tip in the STM simulation setting. This has been theoretically simulated and experimentally observed [61,62]. Notably, although Ru-5f exhibits a high DOS for both spin channels below the Fermi level [see Fig. 5(m)], the signal is predominantly dominated by bridging oxygen atoms rather than Ru-5f (see Figs. 5(a) and 5(c), and SM, Figs. S8(a), S8(b), S8(e), and S8(f) [40]). This occurs because the Ru-5f atoms are located one atomic layer farther from the STM tip compared to the bridging oxygen atoms, resulting in an exponential decrease in tunneling current with distance. Furthermore, the occupied states of the Ru-5f atom contain a large contribution of the in-plane Ru 4d orbitals (see SM, Fig. S8(i) [40]), which do not extend significantly out of plane. This interpretation is further supported by the spin density visualizations shown in SM, Figs. S8(j) and S8(l) [40], revealing that, under negative bias voltages, the spin densities of Ru-6f and O-br cover greater spatial extents than those of Ru-5f.

More importantly, our simulated STM images shown in Fig. 5 reveal clear differences in the spin-dependent images. For example, under negative bias voltages (i.e., probing *occupied* states), we can see high protrusions at Ru-6f and

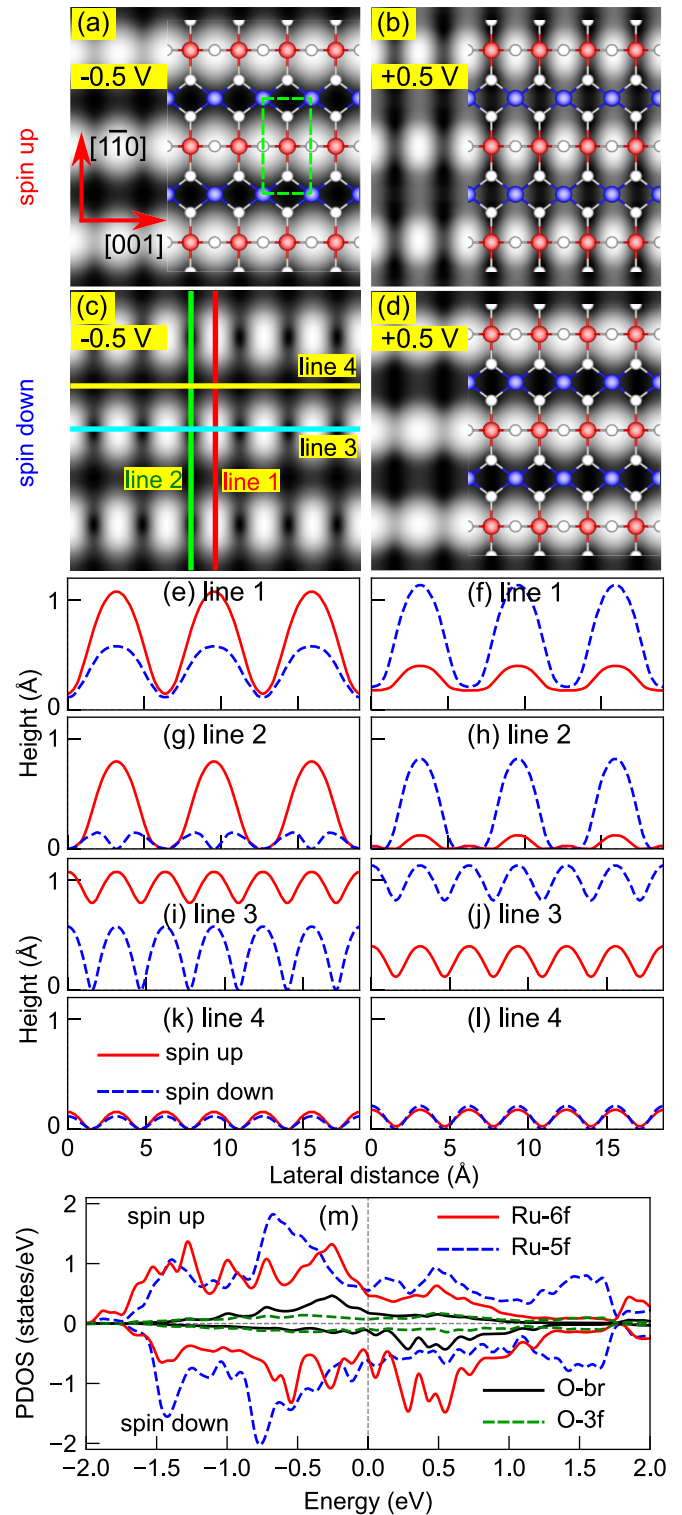


FIG. 5. Simulated STM images of (110) surface. (a)–(d) Images at bias voltages of  $-0.5$  V (left column) and  $+0.5$  V (right column); the unit cell of the surface highlighted by a dashed green rectangle; Ru-6f, Ru-5f, and oxygen atoms represented by red, blue, and bright gray balls, respectively. (e)–(l) Bias- and spin-dependent line profiles indicated as lines 1, 2, 3, and 4 in (c), left and right column figures corresponding to  $-0.5$  V and  $+0.5$  V bias voltages, respectively. (m) Site-projected DOS of surface atoms explaining the difference in spin-dependent images. Atomic labels are denoted as in Fig. 2(b).

O-br positions forming horizontal lines in the spin-up images. This is due to the occupied states being dominated by the majority spin (spin-up) channel, mostly derived from Ru-6f and O-br as identified by the atomic (site-) projected density of states for surface atoms [cf. Fig. 5(m)] and the charge distribution from partial charge density calculations (see SM, Fig. S8(j) vs. Fig. S8(l) [40]). In contrast, when probing the *unoccupied* states under positive bias voltages, higher protrusions forming horizontal lines in the STM images were derived from the spin-down channel.

The spin-dependent feature of the STM images can be clearly corroborated further by the height profiles of the signals scanned over four selected lines indicated in Fig. 5(c). The profile lines displayed in the left-column figures [Figs. 5(e), 5(g), 5(i), and 5(k)] corresponding to the negative bias voltage images exhibit periodic patterns consistent with the dominant contribution of the spin-up densities from Ru-6f and O-br positions. In contrast, the right-column figures [Figs. 5(f), 5(h), 5(j), and 5(l)], representing positive bias voltage scans, show the significant effect of the spin-down densities from the same atomic positions. This aligns well with the expected contribution of the majority and minority spin densities of states in a spin-polarized system.

An intriguing feature emerges when transitioning from negative to positive bias: higher positive biases enhance the visibility of the Ru-5f topography. At +0.5 V bias, the position of Ru-5f becomes discernible in the spin-up images; and at +1.0 V bias, bright vertical columns along  $[1\bar{1}0]$  appearing periodically along the  $[001]$  crystallographic direction are obvious (see SM, Fig. S8(c) [40]). This effect arises from the dominant contribution of the Ru-5f spin-up channel over the spin-down channel in its *unoccupied* states, as demonstrated in Fig. 5(m) and SM, Fig. S8(i) [40]. As the bias voltage increases, the position of Ru-5f atoms becomes more visible due to the higher contribution from the out-of-plane components of its  $4d$  orbitals, as shown in SM, Fig. S8(i) [40], exhibiting a behavior known as contrast reversal. This phenomenon has previously been observed in studies of rutile transition-metal oxide (110) surfaces and helps distinguish

stoichiometric surfaces from other structures under varying experimental conditions, further validating our STM image simulations [62].

#### IV. CONCLUSIONS

In summary, we have shown by first-principles calculations that surface magnetization on RuO<sub>2</sub>(110) emerges from a metallic nonmagnetic bulk RuO<sub>2</sub>. The magnetization is significant at the surface layers and decays quickly as it gets deeper into the bulk region. Symmetry lowering as a result of surface termination induces not only structural relaxation but also significant electronic reorganization at the surface layer, resulting in sizable moments on the atoms forming the surface. This spontaneous surface magnetism proved to exhibit unique properties, including spin-split surface electronic band structure near the Fermi level and distinct spin-resolved spectroscopic features. These findings are expected to provide valuable insights into the interpretation of experimental observations relevant to the magnetic property of RuO<sub>2</sub> in both spectroscopy and transport phenomena, highlighting the pivotal role of surface magnetism in such systems.

#### ACKNOWLEDGMENTS

We thank D. Wickramaratne, J. Xiao, S. Bhatt, and D. Plouff for fruitful discussions. This work was supported by the NSF through the UD-CHARM University of Delaware Materials Research Science and Engineering Center (MRSEC) (Grant No. DMR-2011824). We also acknowledge the use of computational resources from the National Energy Research Scientific Computing Center (NERSC), a Department of Energy Office of Science User Facility, through NERSC Award No. BES-ERCAP 0034471 (m5002), and the DARWIN computing system at the University of Delaware.

#### DATA AVAILABILITY

The data supporting this study's findings are available within the article.

- 
- [1] L. Šmejkal, J. Sinova, and T. Jungwirth, *Phys. Rev. X* **12**, 031042 (2022).
  - [2] L. Šmejkal, R. González-Hernández, T. Jungwirth, and J. Sinova, *Sci. Adv.* **6**, eaaz8809 (2020).
  - [3] Z. Feng, X. Zhou, L. Šmejkal, L. Wu, Z. Zhu, H. Guo, R. González-Hernández, X. Wang, H. Yan, P. Qin *et al.*, *Nat. Electron.* **5**, 735 (2022).
  - [4] S. Karube, T. Tanaka, D. Sugawara, N. Kadoguchi, M. Kohda, and J. Nitta, *Phys. Rev. Lett.* **129**, 137201 (2022).
  - [5] O. Fedchenko, J. Minár, A. Akashdeep, S. W. D'Souza, D. Vasilyev, O. Tkach, L. Odenbreit, Q. Nguyen, D. Kutnyakhov, N. Wind *et al.*, *Sci. Adv.* **10**, eadj4883 (2024).
  - [6] A. Smolyanyuk, I. I. Mazin, L. Garcia-Gassull, and R. Valentí, *Phys. Rev. B* **109**, 134424 (2024).
  - [7] T. Berlijn, P. C. Snijders, O. Delaire, H.-D. Zhou, T. A. Maier, H.-B. Cao, S.-X. Chi, M. Matsuda, Y. Wang, M. R. Koehler *et al.*, *Phys. Rev. Lett.* **118**, 077201 (2017).
  - [8] Z. H. Zhu, J. Stempfer, R. R. Rao, C. A. Occhialini, J. Pellicciari, Y. Choi, T. Kawaguchi, H. You, J. F. Mitchell, Y. Shao-Horn *et al.*, *Phys. Rev. Lett.* **122**, 017202 (2019).
  - [9] M. Hiraishi, H. Okabe, A. Koda, R. Kadono, T. Muroi, D. Hirai, and Z. Hiroi, *Phys. Rev. Lett.* **132**, 166702 (2024).
  - [10] J. Liu, J. Zhan, T. Li, J. Liu, S. Cheng, Y. Shi, L. Deng, M. Zhang, C. Li, J. Ding, Q. Jiang, M. Ye, Z. Liu, Z. Jiang, S. Wang, Q. Li, Y. Xie, Y. Wang, S. Qiao, J. Wen *et al.*, *Phys. Rev. Lett.* **133**, 176401 (2024).
  - [11] P. Keßler, L. Garcia-Gassull, A. Suter, T. Prokscha, Z. Salman, D. Khalyavin, P. Manuel, F. Orlandi, I. I. Mazin, R. Valentí *et al.*, *npj Spintronics* **2**, 50 (2024).
  - [12] L. Kiefer, F. Wirth, A. Bertin, P. Becker, L. Bohatý, K. Schmalzl, A. Stunault, J. A. Rodríguez-Velamazán, O. Fabelo, and M. Braden, *J. Phys.: Condens. Matter* **37**, 135801 (2025).

- [13] M. Wenzel, E. Uykur, S. Rößler, M. Schmidt, O. Janson, A. Tiwari, M. Dressel, and A. A. Tsirlin, *Phys. Rev. B* **111**, L041115 (2025).
- [14] T. Osumi, K. Yamauchi, S. Souma, P. Shubhankar, A. Honma, K. Nakayama, K. Ozawa, M. Kitamura, K. Horiba, H. Kumigashira *et al.*, [arXiv:2501.10649](https://arxiv.org/abs/2501.10649).
- [15] R. M. Sattigeri, G. Cuono, and C. Autieri, *Nanoscale* **15**, 16998 (2023).
- [16] M. Chilcote, A. R. Mazza, Q. Lu, I. Gray, Q. Tian, Q. Deng, D. Moseley, A. Chen, J. Lapano, J. S. Gardner, G. Eres, T. Z. Ward, E. Feng, H. Cao, V. Lauter, M. A. McGuire, R. Hermann, D. Parker, M. Han, A. Kayani *et al.*, *Adv. Funct. Mater.* **34**, 2405829 (2024).
- [17] H. Over, *Chem. Rev.* **112**, 3356 (2012).
- [18] C. Xu, Y. Jiang, D. Yi, H. Zhang, S. Peng, and J. Liang, *J. Am. Ceram. Soc.* **97**, 3702 (2014).
- [19] H. Over, Y. D. Kim, A. P. Seitsonen, S. Wendt, E. Lundgren, M. Schmid, P. Varga, A. Morgante, and G. Ertl, *Science* **287**, 1474 (2000).
- [20] E. Torun, C. M. Fang, G. A. De Wijs, and R. A. De Groot, *J. Phys. Chem. C* **117**, 6353 (2013).
- [21] Q. Liang, A. Bieberle-Hütter, and G. Brocks, *J. Phys. Chem. C* **126**, 1337 (2022).
- [22] M. Uchida, T. Nomoto, M. Musashi, R. Arita, and M. Kawasaki, *Phys. Rev. Lett.* **125**, 147001 (2020).
- [23] J. P. Ruf, H. Paik, N. J. Schreiber, H. P. Nair, L. Miao, J. K. Kawasaki, J. N. Nelson, B. D. Faeth, Y. Lee, B. H. Goodge, B. Pamuk, C. J. Fennie, L. F. Kourkoutis, D. G. Schlom, and K. M. Shen, *Nat. Commun.* **12**, 59 (2021).
- [24] A. K. Rajapitamahuni, S. Nair, Z. Yang, A. K. Manjeshwar, S. G. Jeong, W. Nunn, and B. Jalan, *Phys. Rev. Mater.* **8**, 075002 (2024).
- [25] Y.-Y. Jiang, Z.-A. Wang, K. Samanta, S.-H. Zhang, R.-C. Xiao, W. J. Lu, Y. P. Sun, E. Y. Tsybal, and D.-F. Shao, *Phys. Rev. B* **108**, 174439 (2023).
- [26] Z. Lin, D. Chen, W. Lu, X. Liang, S. Feng, K. Yamagami, J. Osiecki, M. Leandersson, B. Thiagarajan, J. Liu, C. Felser, and J. Ma, *Phys. Rev. B* **111**, 134450 (2025).
- [27] Y. Kobayashi, S. Karube, I. Sugiura, H. Narita, R. Hisatomi, Y. Shiota, and T. Ono, *AIP Adv.* **14**, 115120 (2024).
- [28] P. Hohenberg and W. Kohn, *Phys. Rev.* **136**, B864 (1964).
- [29] W. Kohn and L. J. Sham, *Phys. Rev.* **140**, A1133 (1965).
- [30] P. E. Blöchl, *Phys. Rev. B* **50**, 17953 (1994).
- [31] G. Kresse and D. Joubert, *Phys. Rev. B* **59**, 1758 (1999).
- [32] G. Kresse and J. Furthmüller, *Comput. Mater. Sci.* **6**, 15 (1996).
- [33] G. Kresse and J. Furthmüller, *Phys. Rev. B* **54**, 11169 (1996).
- [34] Certain commercial equipment, instruments, software, or materials are identified in this paper to specify the procedures or equipment used. Such identification is not intended to imply recommendation or endorsement by the National Institute of Standards and Technology, nor is it intended to imply that the materials, equipment, or software identified are necessarily the best available for the purpose.
- [35] J. P. Perdew, K. Burke, and M. Ernzerhof, *Phys. Rev. Lett.* **77**, 3865 (1996).
- [36] J. P. Perdew, K. Burke, and M. Ernzerhof, *Phys. Rev. Lett.* **78**, 1396 (1997).
- [37] S. L. Dudarev, G. A. Botton, S. Y. Savrasov, C. J. Humphreys, and A. P. Sutton, *Phys. Rev. B* **57**, 1505 (1998).
- [38] V. Wang, N. Xu, J.-C. Liu, G. Tang, and W.-T. Geng, *Comput. Phys. Commun.* **267**, 108033 (2021).
- [39] D. L. Burnett, E. Petrucco, K. M. Rigg, C. M. Zaltis, J. G. Lok, R. J. Kashtiban, M. R. Lees, J. D. B. Sharman, and R. I. Walton, *Chem. Mater.* **32**, 6150 (2020).
- [40] See Supplemental Material at <http://link.aps.org/supplemental/10.1103/6fxv-153y> for  $-I_pCOHP$  values for Ru–O bonds in nonmagnetic bulk RuO<sub>2</sub>, local magnetic moment on Ru atoms and layer magnetization upon full relaxation, magnetic moments on magnetic atoms of the outermost-layer as a function of the slab thickness, relative energy of spin-polarized state compared to nonmagnetic state, changes of Bader charges on each atom with respect to those values of the bulk, atom-resolved band structures for surface atoms, layer-resolved band structures for inner layers, momentum and band-resolved spin densities of flat-band near the Fermi level, and simulated STM images of the (110) surface with various bias voltages ranging from  $-1.5$  V to  $+1.5$  V for both spin channels
- [41] R. Dronskowski and P. E. Bloechl, *J. Phys. Chem.* **97**, 8617 (1993).
- [42] V. L. Deringer, A. L. Tchougréeff, and R. Dronskowski, *J. Phys. Chem. A* **115**, 5461 (2011).
- [43] R. Nelson, C. Ertural, J. George, V. L. Deringer, G. Hautier, and R. Dronskowski, *J. Comput. Chem.* **41**, 1931 (2020).
- [44] D. Wortmann, S. Heinze, P. Kurz, G. Bihlmayer, and S. Blügel, *Phys. Rev. Lett.* **86**, 4132 (2001).
- [45] J. Tersoff and D. R. Hamann, *Phys. Rev. B* **31**, 805 (1985).
- [46] D. E. P. Vanpoucke and G. Brocks, *Phys. Rev. B* **77**, 241308(R) (2008).
- [47] P. I. Sorantin and K. Schwarz, *Inorg. Chem.* **31**, 567 (1992).
- [48] R. F. W. Bader, *Atoms in Molecules: A Quantum Theory*, The International Series of Monographs on Chemistry (Clarendon Press, Oxford, 2003), reprinted.
- [49] W. Tang, E. Sanville, and G. Henkelman, *J. Phys.: Condens. Matter* **21**, 084204 (2009).
- [50] R. S. Mulliken, *J. Chem. Phys.* **23**, 1833 (1955).
- [51] P.-O. Löwdin, *J. Chem. Phys.* **18**, 365 (1950).
- [52] C. Ertural, S. Steinberg, and R. Dronskowski, *RSC Adv.* **9**, 29821 (2019).
- [53] G. A. Landrum and R. Dronskowski, *Angew. Chem. Int. Ed.* **39**, 1560 (2000).
- [54] R. Dronskowski, *Int. J. Quantum Chem.* **96**, 89 (2004).
- [55] S. F. Weber, A. Urru, S. Bhowal, C. Ederer, and N. A. Spaldin, *Phys. Rev. X* **14**, 021033 (2024).
- [56] E. C. Stoner, *Proc. R. Soc. Lond. A Math. Phys. Sci.* **165**, 372 (1938).
- [57] V. Jovic, A. Consiglio, K. E. Smith, C. Jozwiak, A. Bostwick, E. Rotenberg, D. Di Sante, and S. Moser, *ACS Catal.* **11**, 1749 (2021).
- [58] V. Jovic, R. J. Koch, S. K. Panda, H. Berger, P. Bugnon, A. Magrez, K. E. Smith, S. Biermann, C. Jozwiak, A. Bostwick, E. Rotenberg, and S. Moser, *Phys. Rev. B* **98**, 241101(R) (2018).

- [59] V. Jovic, R. J. Koch, S. K. Panda, H. Berger, P. Bugnon, A. Magrez, R. Thomale, K. E. Smith, S. Biermann, C. Jozwiak, A. Bostwick, E. Rotenberg, D. D. Sante, and S. Moser, [arXiv:1908.02621](https://arxiv.org/abs/1908.02621).
- [60] S. Heinze, M. Bode, A. Kubetzka, O. Pietzsch, X. Nie, S. Blügel, and R. Wiesendanger, *Science* **288**, 1805 (2000).
- [61] H. Over, M. Knapp, E. Lundgren, A. P. Seitsonen, M. Schmid, and P. Varga, *ChemPhysChem* **5**, 167 (2004).
- [62] T. Feng, Y. Wang, A. Herklotz, M. F. Chisholm, T. Z. Ward, P. C. Snijders, and S. T. Pantelides, *Phys. Rev. B* **103**, 035409 (2021).